Analyst

Accepted Manuscript

This article can be cited before page numbers have been issued, to do this please use: E. Kepes, I. B. Gornushkin, P. Poízka and J. Kaiser, *Analyst*, 2021, DOI: 10.1039/D0AN01996H.

View Article Online
DOI: 10.1039/D0AN01996H

Spatiotemporal spectroscopic characterization of plasmas induced by non-orthogonal laser ablation

Erik Képeš[1,2*], Igor Gornushkin[3], Pavel Pořízka[1,2], Jozef Kaiser[1,2]

[1]Central European Institute of Technology, Brno University of Technology, Purkyňova 656/123, CZ-61200 Brno, Czech Republic

[2]Institute of Physical Engineering, Faculty of Mechanical Engineering, Brno University of Technology, Technická 2, 616 69, Brno, Czech Republic

[3]BAM Federal Institute for Materials Research and Testing, Richard-Willstätter-Strasse 11, 12489 Berlin, Germany

[*]Corresponding author: erik.kepes@ceitec.vutbr.cz

Abstract

Ablation geometry significantly affects the plasma parameters and the consequent spectroscopic observations in laser-induced breakdown spectroscopy. Nevertheless, plasmas induced by laser ablation under inclined incidence angles are studied to a significantly lesser extent compared to plasmas induced by standard orthogonal ablation. However, inclined ablation is prominent in stand-off applications, such as the Curiosity Mars rover, where the orthogonality of the ablation laser pulse cannot be always secured. Thus, in this work, we characterize non-orthogonal ablation plasmas by applying plasma imaging, tomography, and spectral measurements. We confirm earlier observations according to which non-orthogonal ablation leads to a laser-induced plasma that consists of two distinct parts: one expanding primarily along the incident laser pulse and one expanding along the normal of the sample surface. Moreover, we confirm that the former emits mainly continuum radiation, while the latter emits mainly sample-specific characteristic radiation. We further investigate and compare the homogeneity of the plasmas and report that inclined ablation affects principally the ionic emissivity of laser-induced plasmas. Overall, our results imply that the decreased fluence resulting from inclined angle ablation and the resulting inhomogeneities of the plasmas must be considered for quantitative LIBS employing non-orthogonal ablation.

Keywords: laser-induced plasma, laser-induced breakdown spectroscopy, non-orthogonal ablation, plasma tomography, Radon reconstruction

View Article Online
DOI: 10.1039/D0AN01996H

Introduction

Laser-induced breakdown spectroscopy (LIBS) has emerged as one of the most promising in-situ atomic analysis techniques [1–3]. The popularity of LIBS is attributed to its uniquely simple and robust instrumentation. LIBS requires a single laser pulse to vaporize and ionize the sample material, creating a micro-plasma. The collected and spectrally resolved emission produced during the cooling of the plasma can be consequently used for elemental fingerprinting, i.e., for material identification [4–8]. In general, LIBS applies orthogonal ablation. However, in many in-situ applications, the orthogonal angle of incidence of the ablation pulse cannot be ensured. The most prominent example is the ChemCam instrument of the Curiosity Mars rover [9]. In addition, non-orthogonal ablation has been reported to enhance the depth resolution of LIBS during depth profiling [10]. Consequently, several studies have been dedicated to the investigation of the non-orthogonal ablation angles' influence on the LIBS signal. We will henceforth refer to this process as non-orthogonal ablation.

An initial study of the ablation geometry's influence reported that non-orthogonal ablation results in the orthogonal (to the sample surface) ejection of the sample material. Moreover, this was shown to be independent of the incidence angle of the ablation pulse. The observation was attributed to the creation of high-pressure vapors at the ablation spot which, consequently, expand away from this spot along the sample normal [11]. Considering this observation, an extensive study of the influence of collection and ablation angles under simulated Martian atmospheric conditions (predominantly CO_2 atmosphere, 0.009 atm pressure) showed that the ablation angle affects the LIBS signal more significantly than the collection angle [12]. Furthermore, the study confirmed that non-orthogonal ablation results in the partial separation of the plasma emission: The source of the continuum emission propagating along the laser pulse, while the atomic emission expands orthogonally to the sample surface. Thus, a higher signal-to-background ratio can be observed with higher ablation angles. However, higher ablation angles result in a lower laser fluence of the ablation pulse. Nevertheless, the authors reported slightly lower prediction errors (in the context of quantification) with some of the investigated ablation angles compared to orthogonal ablation.

The direction of the plasma's expansion has been further investigated by schlieren imaging [13] and shadowgraphy techniques [14]. Both studies reported that the plasma expands along the incident laser pulse. However, it is important to note that the applied techniques did not provide spectral information about the plasmas. Thus, it is likely that only the expansion of the absorption wave has been observed. On the contrary, according to spectrally resolved studies, the majority of the sample material's emission can be observed along the normal of the sample surface [15,16] despite the plasma expanding along the incident laser pulse.

Apart from the dynamics of the plasma expansion under non-orthogonal ablation, the influence of the incidence angle on the LIBS signal has also been studied. In general, increasing the incidence angle results in the decrease of the fluence of the ablation pulse. However, the ability of LIBS to separate materials was observed not to be significantly affected by ablation angles up to 20° [17]. Moreover, non-orthogonal ablation has been evaluated in terms of impulse coupling, a measure of the momentum delivered into the target proportional to the pulse energy [18]. The authors reported a higher impulse coupling in the case of inclined angle ablation, suggesting less prominent plasma shielding effects compared to orthogonal ablation.

View Article Online
DOI: 10.1039/D0AN01996H

Non-orthogonal ablation and the related laser-induced plasma is also of high interest for various surface sciences. Namely, non-orthogonal ablation is widely employed, e.g., for thin film deposition and material etching. Consequently, non-orthogonal ablation has been extensively studied and characterized in terms of material yield, ionization ratio, and plasma temperature [19–23]. However, as most of these studies have been carried out under high vacuum, the reported results do not directly translate to most LIBS applications, which is subject to atmospheric conditions or low vacuum.

In this work, we characterize plasmas induced by laser pulses with inclined incidence angles. A slight incidence angle of 10° and a somewhat extreme incidence angle of 45° are compared to plasmas induced by the traditional orthogonal ablation. Several ablation energies are explored. The plasmas are compared in terms of apparent expansion angle, atomic and ionic emission, and electron number density and temperature. The temporal evolution of each attribute is determined at various heights above the sample surface. Considering these temporal evolutions, we apply tomographic reconstruction by the Radon-transformation technique to obtain the spatial emissivity distribution at multiple delays after the ablation pulse. The distributions are then used to quantitatively compare the homogeneity of the plasmas.

Methods and Materials

The research was carried out at the Federal Institute for Materials Research and Testing (Berlin, GE) using a unique tomography system which is schematically shown in Figure . The tomography system enables to observe the plasma from variable azimuthal angles. Consequently, the tomographic reconstruction of the whole plasma's white-light emissivity or the tomographic reconstruction of the spectrally resolved emissivity of selected slices of the plasma is possible by applying the Radon transformation technique.

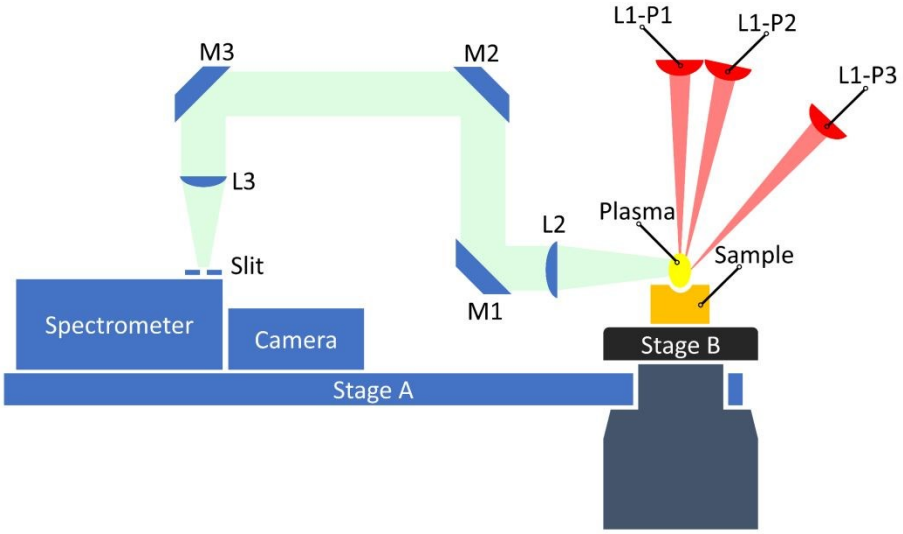

Figure 1 Schematic diagram of the used tomographic system. Stage A – nano-positioning carousel carrying the spectrometer, camera, and collection optics (the blue elements); Stage B – sample stage, capable of translational movement along a single horizontal axis and the vertical axis (x-z axes) and of continuous rotational movement; M1, M2, and M3 – planar mirrors; L1 – plano-convex lens used for focusing the laser beam (f = 100 mm); P1, P2, and P3 – positions of L1 at 0°, 10°, and 45° angles,

View Article Online
DOI: 10.1039/D0AN01996H

respectively, relative to the sample normal; L2 – plano-convex collection lens (f = 75 mm); L3 – plano-convex lens focusing the collimated plasma image onto the spectrometer's slit (f = 100 mm).

Sample

The analyzed sample was selected based on several considerations. Firstly, we aimed at a high temporal resolution, i.e., short exposition times. Secondly, the analyte had to possess emission lines covering a relatively wide range of upper energy states in a narrow spectral window in order to reliably determine the temperature using the Boltzmann plot technique. Thus, we opted for a certified Cu standard (BAM EB38, BAM, GE), and focused our analysis on the matrix lines of Cu I and Cu II. The considered emission lines are listed in Table .

Table 1 List of the considered emission lines. A_{ki} – Einstein coefficient of the transition; E_i – lower energy level involved in the transition; E_k – the upper energy level involved in the transition; and g_k – the degeneracy of the upper energy level. The values were obtained from the NIST atomic spectra database.

	$\mathbf{A_{ki}}\,(\mathbf{10^7\ s^{-1}})$	$\mathbf{E_i}$ (eV)	$\mathbf{E_k}$ (eV)	$\mathbf{g_k}$
Cu I 510.55 nm	0.2	1.39	3.82	7
Cu I 515.32 nm	6.0	3.79	6.19	4
Cu I 521.82 nm	7.5	3.82	6.19	6
Cu II 329.04 nm	5.9	14.33	18.10	13
Cu II 330.79 nm	5.6	14.62	18.36	9

Laser ablation

The plasmas were induced with a Brilliant Eazy Twins (Quantel laser, FR) single-pulse Nd:YAG laser system with a wavelength of 1064 nm. The collimated laser pulse was focused by using a single plano-convex lens with a focal length of 100 mm lens (Thorlabs, Inc., USA) with a lens-to-sample distance of 100 mm (L1 in Figure). The laser pulse energy was measured prior to the focusing lens. In total, three ablation energies (15, 55, and 80 mJ) were studied, each in three distinct zenithal ablation angles (0°, 10°, and 45° relative to the surface normal (P1, P2, and P3, respectively, in Figure). The measured fluctuation of the laser pulse energy was ±5%. The diameter of the laser spot in the case of orthogonal incidence was (400 ± 20) µm. The pulse length was 5 ns. Single shots with a Gaussian profile were used. A clean sample surface was exposed to each shot. In the case of non-orthogonal ablation, the laser spot is elongated along a single axis. Hence, the final spot shape is elliptical. The length of the elongated axis is $\frac{d}{\cos(\theta)}$, which in the case of the $\theta = 10°$ and $\theta = 45°$ ablation angles enumerates to 1.5% and 41%, respectively, compared to the orthogonal ablation with a spot diameter of d.

Plasma imaging and spectral acquisition

The plasma emission was collected with a single plano-convex lens with a focal length of 75 mm (Thorlabs, Inc., USA) placed 75 mm from the plasma. The collimated light was guided by three planar mirrors and finally projected onto the slit of a Czerny–Turner-type monochromator (Acton 2500i, Princeton Instruments, Inc., USA) using a single lens with a focal length of 100 mm, yielding a magnification of 1.3. For spectrally resolved measurements, a 1200 grooves/mm grating was used. For white-light imaging experiments, the same grating was used in its zeroth order. The images were

View Article Online
DOI: 10.1039/D0AN01996H

recorded using an ICCD camera (PI-MAX2, Princeton Instruments, Inc., USA) with a pixel size of 26×26 μm^2, and a resolution of 512×512 pixels. The laser's flashlamp and Q-switch were triggered with a DG645 type delay generator (Stanford Research Systems, USA). Meanwhile, the timing of the photocathode, multichannel plate, and the read-out of the camera were controlled by a DG535 type delay generator (Stanford Research Systems, USA). In addition, the DG535 was triggered externally by the DG645. For white-light imaging experiments, the monochromator's slit was fully open, resulting in a 3 mm slit width. For spectrally resolved experiments, the slit width was 100 µm, corresponding to an approximately 75 µm wide slice of the plasma which was parallel to the sample surface. Spectrally resolved measurements were performed for slices 0.2 mm and 0.5 mm above the sample surface. For both the white-light and spectrally resolved imaging experiments, an exposure time (commonly referred to as gate width) of 10 ns was used. Both white-light and spectrally resolved measurements were carried out at various (gate) delays after the ablation pulse (t_d), which are further specified in the text. Owing to the limited spectral range of the monochromator (20 nm wide spectral window), the ionic and atomic emission was recorded separately, using spectral windows centred at 330 nm and 518 nm, respectively. An example of the former is shown in Figure S1 (Supplementary materials), which demonstrates the calculation of the emission lines' intensity. Namely, the major emission lines in the recorded spectral range were fitted by a Lorentzian profile. A constant baseline value was considered during fitting. The area under the fitted emission line was considered as its intensity.

Image processing and tomographic reconstruction

For each measurement (both white-light and spectrally resolved), 10 images were recorded. Baseline subtraction was applied to each individual image according to the following procedure: The images' region outside of the slit's image was considered as the dark current signal. Hence, the intensity in this region was averaged and subtracted from the whole image. Moreover, values lower than three times the standard deviation of the dark current regions' signal were set to zero. Lastly, for spectrally resolved experiments, the continuum signal (determined by fitting the intensity values at the two shoulders of a selected emission line by a linear model) was also subtracted. For the tomographic reconstructions, images were collected with a 5° angular resolution. Hence, 38×10 images were collected for each reconstruction in the range of 0–185°. The tomographic reconstruction was carried out using the Radon transformation technique, which has been described in detail for LIBS applications before [24–26].

Error estimation

The error of the measurements was determined by an iterative bootstrapping approach. For each angular position, ten iterations were performed. In each iteration, the ten images recorded at an angular position were sampled with replacement, which yielded n sampled images. The sampled n images could include the same recorded image several times. Subsequently, the n sampled images were averaged to obtain a single average image in each iteration. Lastly, an estimate of the standard deviation of the averaged images (obtained from the 10 separate iterations) was calculated at each angular position. However, this estimate is lower than the true standard deviation by a factor of $\sqrt{n}$ [27]. We used $n = 10$ in this work. Consequently, the standard deviation determined by the bootstrapping approach multiplied by $\sqrt{10}$ was considered as the final error of the measurement.

View Article Online
DOI: 10.1039/D0AN01996H

Plasma characterization

The plasmas were characterized in terms of atomic and ionic emission (Cu I and Cu II, respectively), electron number density and temperature, expansion angle, and ionization fraction. The electron temperature was determined by the Boltzmann plot technique [28], using the Cu I lines listed in Table . The determined temperature values were consequently combined with the Cu I/Cu II ratio (Cu I 521 nm and Cu II 330 nm from Table) to determine the electron number density considering the Saha–Boltzmann equilibrium [29]. The intensity of the emission lines was determined as their integrated area. The optical thinness of the emission lines was verified by the duplicating mirror approach [30]. The expansion angle was estimated by fitting the row-wise maxima of the white-light images by a straight line. Consequently, the angle between the resulting line and the sample normal was considered as the expansion angle. According to previous reports, this expansion angle corresponds to the absorption wave [15]. The expansion angle of the ablated sample material was inferred from the spectrally resolved tomographic reconstructions. The ionization fraction α was calculated as [31,32]:

$$\alpha = \frac{1}{1 + \frac{k_{Saha}}{n_e}} \quad (1)$$

where n_e is the electron number density, and

$$k_{Saha} = \frac{(2\pi m_e k_B T)^{\frac{3}{2}} 2U^i}{h^3 \quad U^n} e^{-\frac{E_{ion}}{k_B T}} \quad (2)$$

where m_e is the rest mass of the electron, k_B is the Boltzmann constant, h is the Planck constant, U^i and U^n are the partition functions of the ionic and neutral emission lines, respectively, and E_{ion} is the ionization potential.

Results and discussion

All the white-light images obtained with an ablation energy of 80 mJ are provided as Supplementary materials. A subset of the images is shown in Figure , where the white-light intensity of the plasmas induced under the three investigated incidence angles is compared at various delays after the laser irradiation. The images were recorded orthogonally to the ablation pulses' plane of propagation. According to these figures, the laser-induced plasma initially expands along the incident laser pulse. However, with the increasing delay, the plasma expansion straightens. As there are no external forces acting on the plasma that could result in such a change of morphology, the plasma is likely composed of two segments with distinct lifetimes. Indeed, this corresponds to earlier reports of the continuum emission propagating along the laser pulse. It has been shown that the plasma expanding along the incident laser pulse mainly emits continuum radiation generated by Bremsstrahlung and ion-electron recombination processes [12].

The lifetime of the continuum is shorter than that of the characteristic radiation [33]. Consequently, the apparent straightening of the plasma is the result of the decreasing of the continuum radiation. This is confirmed by determining the apparent expansion angle of the plasma. An example is shown in Figure

View Article Online
DOI: 10.1039/D0AN01996H

(a) for the 80 mJ ablation energy and 10° ablation angle, while the temporal evolution of the expansion angles determined for the remaining ablation parameters is included as Supplementary materials. In addition, the emission in the 508—528 nm spectral range that contains three Cu I emission lines (Table) is shown in Figure (b). The presented t_d values correspond to the apparent straightening of the plasma expansion.

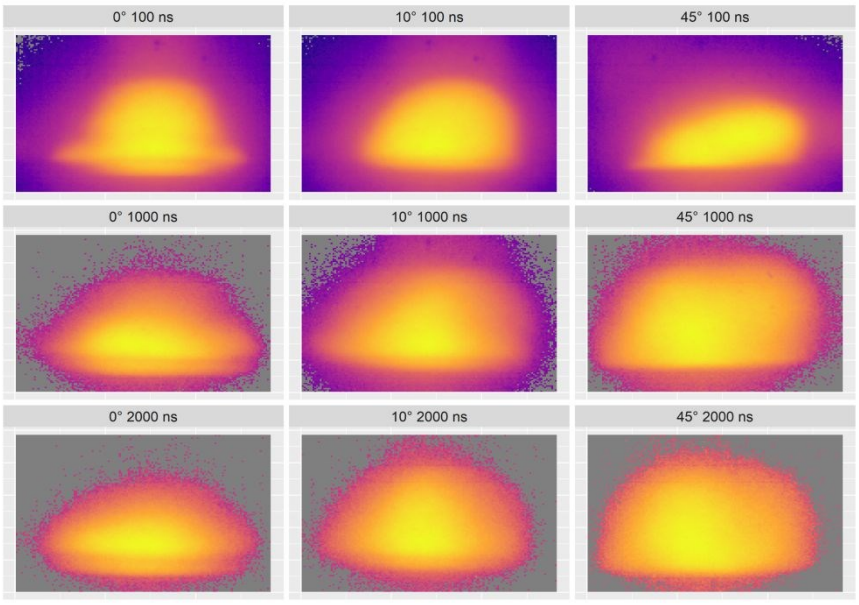

Figure 2 White-light emissivity images of plasmas induced by non-orthogonal ablation with a pulse energy of 80 mJ. Each image was individually normalized to the 0—1 range.

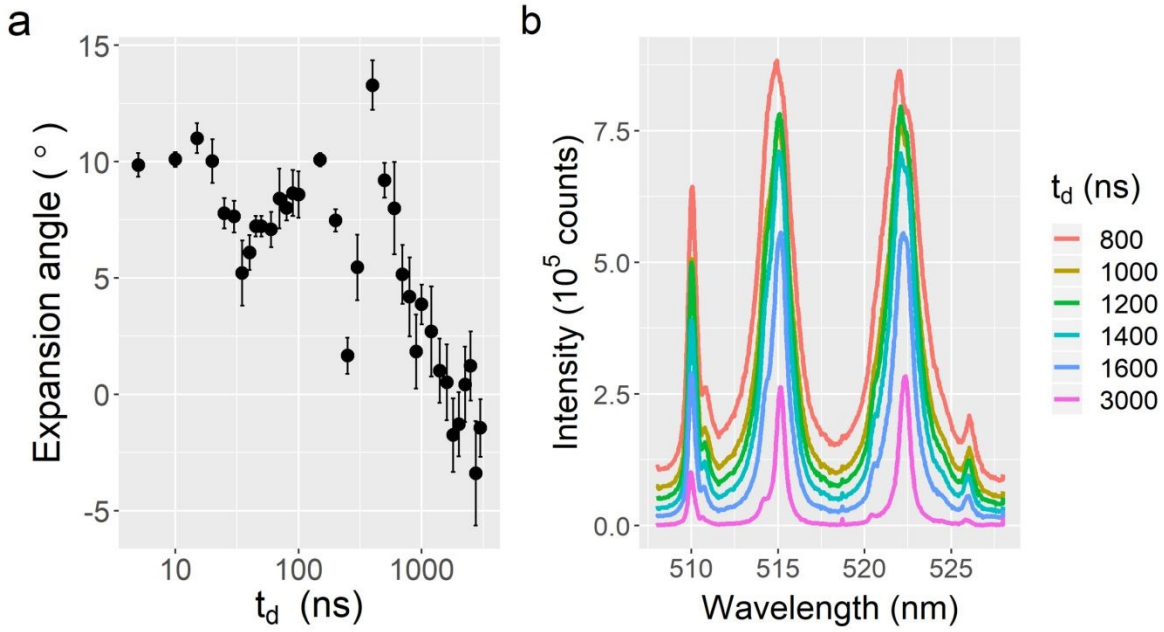

Figure 3 (a) Determined apparent expansion angle and (b) corresponding emission spectra for 10° incidence angle and 80 mJ ablation energy. The error bars have been determined following the process described in the Methods and Materials section. t_d – delay after the ablation pulse.

View Article Online
DOI: 10.1039/D0AN01996H

The orthogonal expansion of the sample material is further supported by tomographic reconstructions. Abel transformation was applied in the case of orthogonal ablation, and Radon transformation in the case of non-orthogonal ablation. An example of the reconstructed emissivities is shown in Figure (additional figures showing the emissivity distributions at various heights above the sample surface and delay values are provided as Supplementary materials). Figure shows the reconstructed emissivity distribution of the Cu I 521 nm emission line in the horizontal plane 0.2 mm above the sample surface for various ablation energies and incidence angles. Hence, superior symmetry of the orthogonally ablated plasmas' emissivity (top row in Figure) is primarily caused by the transformation's fundamental assumption of radial symmetry. Nevertheless, despite the asymmetry exhibited by non-orthogonal ablation plasmas, the overall distributions are comparable. Moreover, the centers of the distributions approximately coincide, i.e., despite the change in incidence angles and the resulting changes in the apparent expansion angles, the sample material's emissivity remains aligned with the emissivity observed for orthogonal ablation.

Consequently, it is evident that, as concluded by earlier reports, the sample material expands along the sample normal, similarly to the case of orthogonal ablation. Nevertheless, the emission of the sample plasma might exhibit differences. Hence, we investigated the spatially integrated atomic and ionic intensities, the electron temperature, and electron number density along two distinct slices of the plasmas located at 0.2 and 0.5 mm above the sample surface. The results for the ablation energy of 80 mJ are shown in Figure (other examples are included as Supplementary materials).

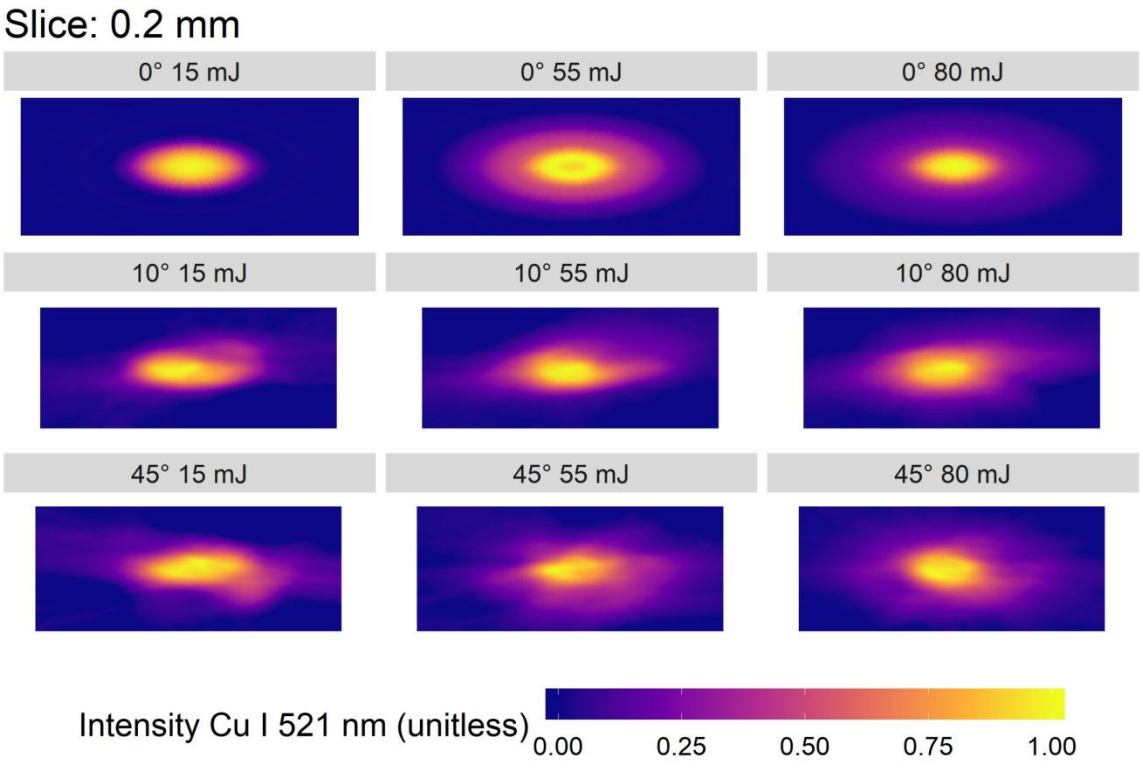

Figure 4 Reconstructed Cu I 521 nm emissivity in the horizontal plane 0.2 mm above the sample surface for plasmas induced with various ablation energies and incidence angles 1000 ns after ablation. The emissivity distributions have been individually normalized to the 0—1 range. Thus, the shown values are unitless.

View Article Online
DOI: 10.1039/D0AN01996H

As expected, orthogonal ablation results in the highest emission line intensities, temperature, and electron number density. Note that the slightly higher temperature observed in the case of the 10° incidence angle compared to that of the orthogonal ablation is well within the estimated uncertainty of the results of 15%. Similar temperatures (in the order of 1E+4 K) have been commonly reported for orthogonal ablation with pulse energies ranging from 20 mJ to 200 mJ [34–38], which validates our results. Overall, the observed temporal evolution of the temperature is in good agreement with existing reports [39–43]. In addition, for each plasma, the ionization fraction calculated according to (1,2) approached unity, which is in line with studies of orthogonal ablation [44]. On the contrary, in the case of non-orthogonal ablation lower ionization fractions have been reported [19]. However, the latter were obtained under vacuum. Hence, there is no direct contradiction between the reported results and ours. Moreover, the difference in emission intensities between the two slices (0.2 and 0.5 mm, marked with circles and triangles, respectively) observed for the orthogonal ablation and the 10° incidence angle is also similar. On the contrary, the plasma induced by the 45° incidence angle exhibits a higher degree of homogeneity compared to the other two incidence angles, i.e., the emission intensity profiles at the two slices coincide to a larger extent. However, the decrease of the laser fluence resulting from the 45° incidence angles (approximately 41%) leads to a significant reduction in the overall intensity. Meanwhile, the 10° ablation angle results in an approximately 1.5% fluence reduction. Considering the exponential decrease of the electron number density and temperature seen in Figure , the spatial distribution of both atomic and ionic emissivity was further investigated at three distinct delays after the ablation pulse: at the top, middle, and bottom of the exponential curve.

View Article Online
DOI: 10.1039/D0AN01996H

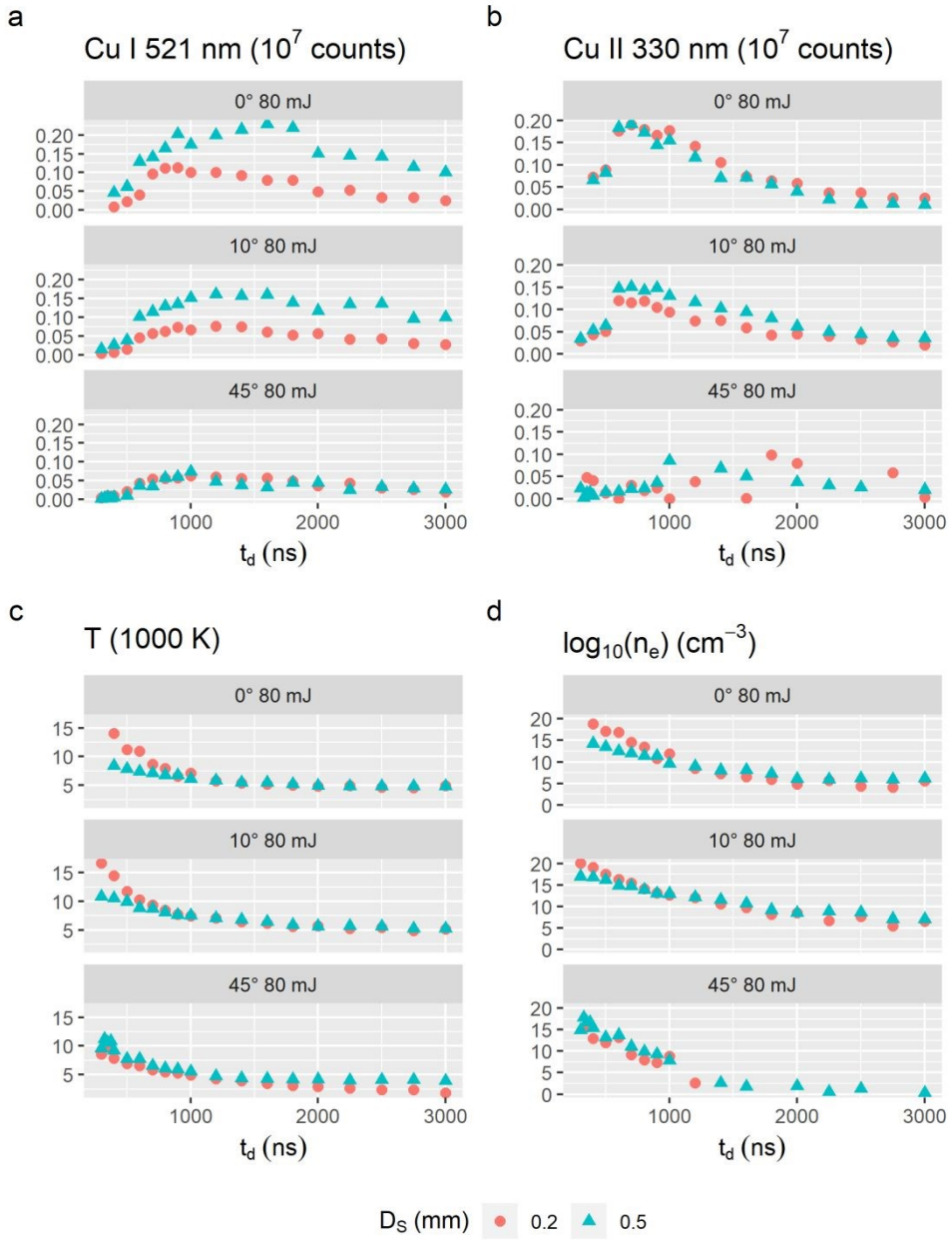

Figure 5 (a) Atomic emission intensity; (b) Ionic emission intensity; (c) electron temperature; and (d) electron number density of the plasmas at two distinct heights above the sample surface for three incidence angles and ablation energy of 80 mJ. The estimated error of the values is 15 %. t_d – delay after the laser ablation pulse, D_s – height of the slice above the sample surface. Each point was obtained from a different laser shot. Each laser shot was exposed to a clean sample surface.

View Article Online
DOI: 10.1039/D0AN01996H

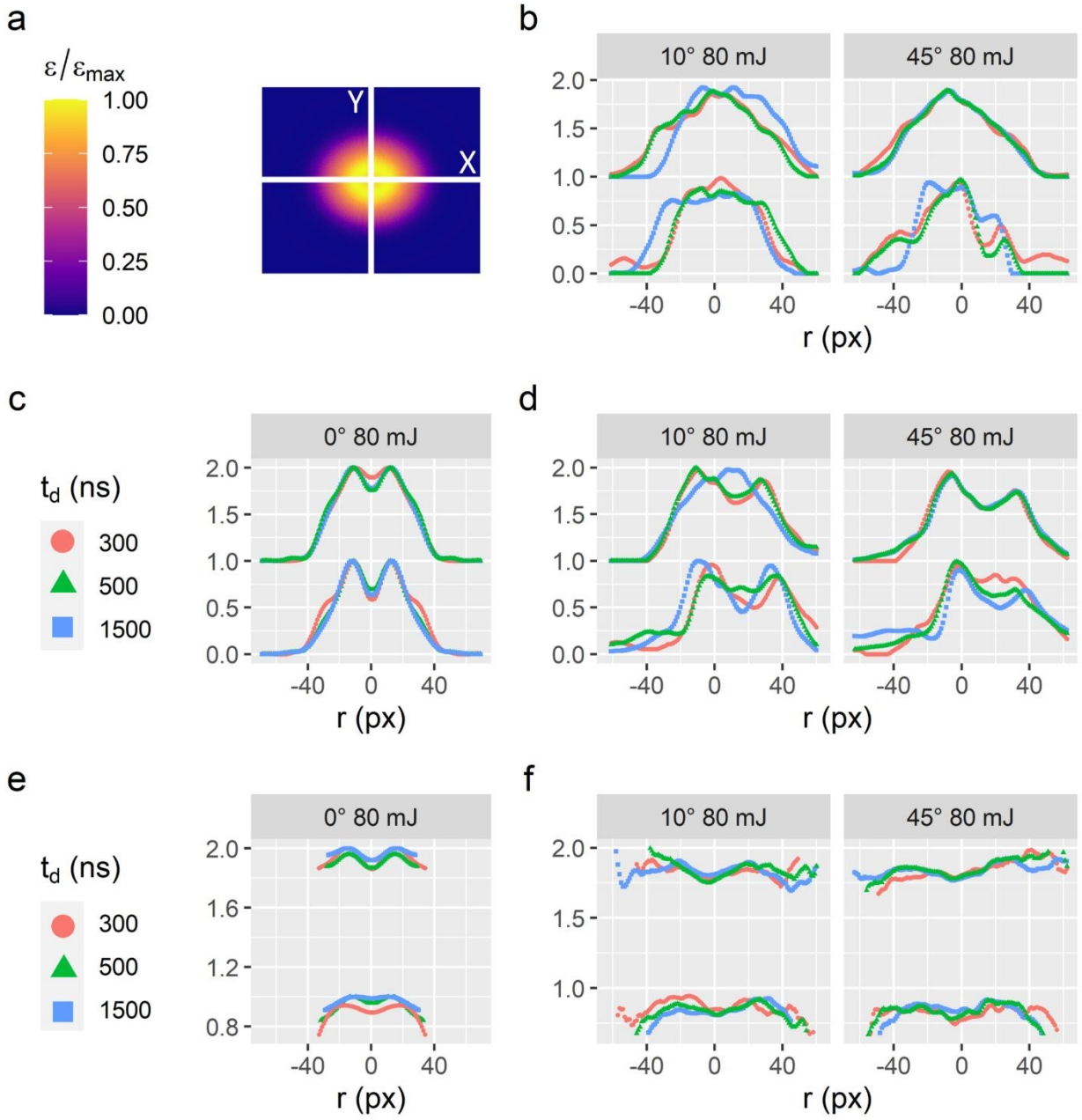

Figure 6 Distribution of (a) the Cu I 521 nm emissivity at orthogonal ablation and 80 mJ ablation energy; (b) Cu I 521 nm emissivity profiles along the X axis marked in (a) for inclined angle ablation (ablation parameters are shown in the figure)); (c) Cu I 521 nm emissivity profiles along the X axis corresponding to (a); (d) Cu I 521 nm emissivity profiles along the Y axis marked in (a) for inclined angle ablation; (e) and (f) electron number density profiles corresponding to the X axis marked in (a). ε – emissivity, ε_{max} – maximum emissivity, t_d – delay after the ablation pulse (marked by the different colors). The different t_d values refer to the top, middle, and bottom of the exponential decay of the electron number density's temporal evolution. The ablation angle propagated along the X axis from the right side.

Considering the superior homogeneity of the orthogonally ablated plasmas that results from using the Abel transform (which takes advantage of the axial symmetry of orthogonal plasmas), the homogeneity of the emissivities was evaluated only along the radial direction of the cross-sections (Figure) rather than the whole distribution. Examples of the (resulting) Abel- and Radon-inverted atomic emissivity

View Article Online
DOI: 10.1039/D0AN01996H

profiles are shown in Figure , where the emissivity profiles have been normalized to the 0—1 range. Moreover, to enhance the visibility, the emissivity profile of the top slice (located 0.5 mm above the sample surface) was moved vertically by 1. The emissivity profiles obtained for orthogonal ablation are in good agreement with those predicted by theoretical models [45]. According to Figure , the emissivity profiles significantly vary between the two axes of observation (X,Y) and even between the two horizontal slices (0.2, 0.5 mm above the sample surface). These discrepancies are quantified by two approaches. To evaluate the homogeneity of the plasmas along the sample normal (vertical homogeneity), the correlation between the profiles at 0.2 and 0.5 mm above the sample surface was calculated. On the contrary, to evaluate the homogeneity of the plasmas along the sample surface, the characteristic length ℓ_S was calculated for each profile separately. The characteristic length ℓ_S of species S is defined as[26]:

$$\ell_S = \frac{\langle \varepsilon_S \rangle}{\left\langle \left| \frac{\partial \varepsilon_S}{\partial r} \right| \right\rangle} \quad (3)$$

where ε_S is the emissivity of species S, $\frac{\partial}{\partial r}$ is the partial derivative along the radial direction r (either $r = X$ or $r = Y$ directions shown in Figure (a)), $\langle A \rangle$ is the mean of the quantity A. S can be any of the emission lines listed in Table 1.

A longer characteristic length corresponds to a more uniform emissivity. The results are shown in Table . However, for brevity, the table contains only the mean values for a single representative atomic (Cu I 521 nm) and a single ionic (Cu II 330 nm) line, and the corresponding standard deviations. Similar results were observed for the remaining emission lines in Table . Note that the mean values (and the corresponding relative standard deviations) were calculated from the two profiles (in the X and Y directions in Figure a) observed at various delays individually for the two horizontal slices, i.e., the mean values were calculated from six values for each horizontal slice. Thus, the relative standard deviations (relative to the mean characteristic lengths) presented in Table correspond to the temporal change of the plasmas, while the mean values are related to the horizontal homogeneity.

Consequently, according to the results presented in Table , several conclusions can be made. The vertical homogeneity (expressed by the correlation values) of the atomic emission is significantly affected only by large incidence angles and low ablation energies (45° at 15 mJ). The remaining ablation parameters did not result in a statistically significant deviation for the values observed with orthogonal ablation. On the contrary, the vertical homogeneity of the ionic emissivity profiles is significantly reduced by even a small deviation from the orthogonal incidence angle. This is likely caused by the ionization predominantly taking place at the shockwave boundaries [46]. As discussed earlier and according to existing reports [13,14], the shockwave created by non-orthogonal ablation is more complex than the one created by orthogonal ablation. Consequently, the less homogeneous ionic emissivity profiles with respect to the orthogonal case likely result from the different height dependency of the interaction of the laser radiation with the shockwave. Nevertheless, these claims require further investigation.

Considering mean characteristic length values in Table , the plasmas exhibit comparable horizontal emissivity homogeneities for atoms. However, non-orthogonal ablation resulted in slightly more homogeneous ionic emissivity profiles compared to orthogonal ablation. On the contrary, orthogonal ablation yields temporally more stable plasmas, as shown by the lower relative standard deviation

View Article Online
DOI: 10.1039/D0AN01996H

values. Lastly, the opposite trend in temporal homogeneity exhibited by the 10° and 45° ablation angles must be pointed out. The fastest change in emissivity exhibited by the 10° ablation angle was observed with the lowest ablation energy for both atomic and ionic emissivities but with the highest energy in the case of the 45° ablation angle. This is likely the result of the overall low ionic emissivity observed for 15 and 55 mJ ablation energies because of which the inhomogeneities of the emissivity profiles fall below our ability to resolve them. Lastly, the apparent non-homogeneity of the distribution of the emitting species in the plasma might result in self-absorption. Consequently, the intensity of the emission lines obtained at different angular positions was compared. Since significant inhomogeneities have been observed only along a single radial direction (direction X in Figure (a)), self-absorption would result in a decreased emission line intensity with the varying observation angle. Nevertheless, no noticeable self-absorption was observed.

In addition to the reconstructed emissivity profiles, Figure (e) and 6(f) show examples of the reconstructed electron number densities. A slight increase of electron number density can be observed towards the incoming ablation pulse at 0.5 mm above the sample surface in the case of the 45° incidence angle. This is likely the result of the gradient of ablation pulse's electric field, which is more prominent at larger distances from the sample surface and larger incidence angles.

Table 2 Figures of merit characterizing the spatial and temporal homogeneity of the plasmas induced by various ablation parameters: θ_{inc} – ablation pulse's incidence angle, E_{abl} – ablation energy. cor_S – correlation between the emissivity profiles of S at 0.2 and 0.5 mm above the sample surface; $\langle \ell_S \rangle$ and $\Delta_r \ell_S$ – mean characteristic length of the S emissivity profiles (defined in the text) and the corresponding relative standard deviation, respectively. $S \in \{\text{Cu I } 521 \text{ nm}, \text{Cu II } 330 \text{ nm}\}$

$\theta_{inc}(°)$	E_{abl} (mJ)	$cor_{Cu\ I}$	$cor_{Cu\ II}$	$\langle \ell_{Cu\ I} \rangle$	$\Delta_r \ell_{Cu\ I}$	$\langle \ell_{Cu\ II} \rangle$	$\Delta_r \ell_{Cu\ II}$
0	15	0.97	0.97	22.6	0.13	19.4	0.12
	55	0.96	0.99	24.3	0.13	19.8	0.13
	80	0.99	0.99	22.3	0.11	20.1	0.11
10	15	0.97	0.92	20.4	0.28	24.4	0.22
	55	0.98	0.90	22.6	0.17	27.2	0.16
	80	0.97	0.81	20.8	0.17	25.8	0.14
45	15	0.92	0.81	24.7	0.18	23.7	0.16
	55	0.97	0.92	23.1	0.17	26.9	0.18
	80	0.96	0.89	22.4	0.18	23.5	0.24

Conclusion

In this work, we presented the characterization of plasmas induced by non-orthogonal laser ablation and compared them to plasmas induced by orthogonal ablation. For each incidence angle, multiple ablation energies were explored. Our investigation mainly focused on the possible influence of non-orthogonal ablation on the homogeneity of laser-induced plasmas' atomic and ionic emissivity.

Considering white-light emissivity, the plasmas induced by non-orthogonal ablation were observed to initially expand along the incident ablation pulse and subsequently "straighten", i.e., their apparent expansion angle got aligned with the sample surfaces normal vector approximately 2 μs after ablation. However, the non-orthogonal expansion of the initial plasma was concluded to be caused by the division of the laser-induced plasma into two parts: a part following the ablation pulse, which mainly emits

View Article Online
DOI: 10.1039/D0AN01996H

continuous radiation, and a part composed of the sample material expanding along the sample normal. Consequently, the faster decrease of the background radiation compared to that of the characteristic radiation results in the apparent straightening of the plasma.

The temporal evolution of the plasmas' atomic and ionic emission, temperature, and electron number density exhibited comparable trends. Similarly, non-orthogonal ablation was observed to have no detrimental effects on the overall morphology of the sample plasma. However, the homogeneity of the plasma emissivity was noticeably affected. Moreover, the emissivity of ionic species was observed to be affected to a larger extent, likely caused by the shockwave's role in the ionization.

Thus, the possibility to separate the background radiation from the sample material's emission by using non-orthogonal ablation is greatly limited: Firstly, considering the high incidence angles required to achieve a reasonable separation, the energy of the ablation pulses would have to be greatly increased compared to commonly used values. Secondly, inclined angle ablation affects the homogeneity of the plasma, especially along the direction of the ablation pulse's elongation. These changes must be taken into consideration if quantitative analysis is attempted using non-orthogonal ablation.

Acknowledgement

The authors acknowledge the financial support of the Ministry of Education, Youth and Sports of the Czech Republic (MEYS CR) under the project CEITEC 2020 (LQ1601) and the CzechNanoLab Research Infrastructure supported by MEYS CR (LM2018110). EK is grateful for the support provided by the Brno Ph.D. Talent program and the grant CEITEC VUT-J-20-6482 from the Brno University of Technology. The authors are grateful to Prof. U. Panne and Dr. K. Rurack for their support of this project.

References

1 R. Noll, C. Fricke-Begemann, S. Connemann, C. Meinhardt and V. Sturm, J. Anal. At. Spectrom., 2018, **33**, 945–956.

2 Z.-Z. Wang, Y. Deguchi, Z.-Z. Zhang, Z. Wang, X.-Y. Zeng and J.-J. Yan, Front. Phys., 2016, **11**, 114213.

3 R. E. Russo, X. Mao, H. Liu, J. Gonzalez and S. S. Mao, Talanta, 2002, **57**, 425–451.

4 D. A. Cremers and L. J. Radziemski, Handbook of Laser-Induced Breakdown Spectroscopy, John Wiley & Sons Ltd, Oxford, UK, 2013.

5 D. W. Hahn and N. Omenetto, Appl. Spectrosc., 2010, **64**, 335A-336A.

6 D. W. Hahn and N. Omenetto, Appl. Spectrosc., 2012, **66**, 347–419.

7 A. W. Miziolek, V. Palleschi and I. Schechter, Laser-Induced Breakdown Spectroscopy (LIBS) : Fundamentals And Applications, Cambridge University Press, 2006.

8 R. Noll, Laser-Induced Breakdown Spectroscopy, Springer Berlin Heidelberg, Berlin, Heidelberg, 2012.

9 R. C. Wiens, S. Maurice, B. Barraclough, M. Saccoccio, W. C. Barkley, J. F. Bell, S. Bender, J. Bernardin, D. Blaney, J. Blank, M. Bouyé, N. Bridges, N. Bultman, P. Caïs, R. C. Clanton, B. Clark, S.

View Article Online
DOI: 10.1039/D0AN01996H

Clegg, A. Cousin, D. Cremers, A. Cros, L. Deflores, D. Delapp, R. Dingler, C. D'Uston, M. Darby Dyar, T. Elliott, D. Enemark, C. Fabre, M. Flores, O. Forni, O. Gasnault, T. Hale, C. Hays, K. Herkenhoff, E. Kan, L. Kirkland, D. Kouach, D. Landis, Y. Langevin, N. Lanza, F. Larocca, J. Lasue, J. Latino, D. Limonadi, C. Lindensmith, C. Little, N. Mangold, G. Manhes, P. Mauchien, C. McKay, E. Miller, J. Mooney, R. V. Morris, L. Morrison, T. Nelson, H. Newsom, A. Ollila, M. Ott, L. Pares, R. Perez, F. Poitrasson, C. Provost, J. W. Reiter, T. Roberts, F. Romero, V. Sautter, S. Salazar, J. J. Simmonds, R. Stiglich, S. Storms, N. Striebig, J. J. Thocaven, T. Trujillo, M. Ulibarri, D. Vaniman, N. Warner, R. Waterbury, R. Whitaker, J. Witt and B. Wong-Swanson, Space Sci. Rev., 2012, **170**, 167–227.

10 C. C. García, M. Corral, J. M. Vadillo and J. J. Laserna, Appl. Spectrosc., 2000, **54**, 1027–1031.

11 R. A. Multari and D. A. Cremers, IEEE Trans. Plasma Sci., 1996, **24**, 39–40.

12 E. A. Breves, K. Lepore, M. D. Dyar, S. C. Bender, R. L. Tokar and T. Boucher, Spectrochim. Acta Part B At. Spectrosc., 2017, **137**, 46–58.

13 J. J. Chang and B. E. Warner, Appl. Phys. Lett., 1996, **69**, 473–475.

14 T. Liu, X. Gao, Z. Hao, Z. Liu and J. Lin, J. Phys. D. Appl. Phys., 2013, **46**, 485207.

15 A. Ilyin, I. Nagorny and Y. Biryukova, Appl. Mech. Mater., 2015, **723**, 825–828.

16 R. A. Multari, L. E. Foster, D. A. Cremers and M. J. Ferris, Appl. Spectrosc., 1996, **50**, 1483–1499.

17 C. López-Moreno, S. Palanco and J. J. Laserna, J. Anal. At. Spectrom., 2007, **22**, 84–87.

18 X.-T. Zhao, F. Tang, B. Han and X.-W. Ni, J. Appl. Phys., 2016, **120**, 213103.

19 L. Torrisi, Radiat. Eff. Defects Solids, 2002, **157**, 347–356.

20 F. Caridi, L. Torrisi, D. Margarone and A. Borrielli, Radiat. Eff. Defects Solids, 2008, **163**, 357–363.

21 L. Torrisi, D. Margarone, A. Borrielli and F. Caridi, Appl. Surf. Sci., 2008, **254**, 4007–4012.

22 L. Torrisi, F. Caridi, D. Margarone, A. Picciotto, A. Mangione and J. J. Beltrano, Appl. Surf. Sci., 2006, **252**, 6383–6389.

23 L. Torrisi, S. Gammino, A. Picciotto, D. Margarone, L. Laska, J. Krasa, K. Rohlena and J. Wolowski, Rev. Sci. Instrum., 2006, **77**, 03B708.

24 S. Merk, S. V. Shabanov, I. B. Gornushkin and U. Panne, J. Anal. At. Spectrom., 2011, **26**, 2483.

25 I. B. Gornushkin, S. Merk, A. Demidov, U. Panne, S. V. Shabanov, B. W. Smith and N. Omenetto, Spectrochim. Acta Part B At. Spectrosc., 2012, **76**, 203–213.

26 S. Eschlböck-Fuchs, A. Demidov, I. B. Gornushkin, T. Schmid, R. Rössler, N. Huber, U. Panne and J. D. Pedarnig, Spectrochim. Acta Part B At. Spectrosc., 2016, **123**, 59–67.

27 E. Képeš, P. Pořízka and J. Kaiser, J. Anal. At. Spectrom., 2019, **34**, 2411–2419.

28 H. R. Griem, Principles of Plasma Spectroscopy, Cambridge University Press, 1997.

29 A. P. Thorne, Spectrophysics, Springer Netherlands, Dordrecht, 1988.

30 H.-Y. Moon, K. K. Herrera, N. Omenetto, B. W. Smith and J. D. Winefordner, Spectrochim. Acta

View Article Online
DOI: 10.1039/D0AN01996H

Part B At. Spectrosc., 2009, **64**, 702–713.

31 D. W. Hahn and N. Omenetto, Appl. Spectrosc., 2012, **66**, 347–419.

32 P. W. J. M. Boumans, Theory of Spectrochemical Excitation, Springer US, Boston, MA, 1995.

33 V. Hohreiter, J. E. Carranza and D. W. Hahn, Spectrochim. Acta Part B At. Spectrosc., 2004, **59**, 327–333.

34 N. Farid, S. Bashir and K. Mahmood, Phys. Scr., 2012, **85**, 015702.

35 Y.-I. Lee, K. Song, H.-K. Cha, J.-M. Lee, M.-C. Park, G.-H. Lee and J. Sneddon, Appl. Spectrosc., 1997, **51**, 959–964.

36 M. Hanif, M. Salik and M. A. Baig, Opt. Lasers Eng., 2011, **49**, 1456–1461.

37 R. Gaudiuso, M. Dell'Aglio, O. De Pascale, A. Santagata and A. De Giacomo, Spectrochim. Acta Part B At. Spectrosc., 2012, **74–75**, 38–45.

38 A. P. Rao, M. Gragston, A. K. Patnaik, P. S. Hsu and M. B. Shattan, Opt. Express, 2019, **27**, 33779.

39 E. Asamoah and Y. Hongbing, Appl. Phys. B, 2017, **123**, 22.

40 J. Wang, H. Fu, Z. Ni, X. Chen, W. He and F. Dong, Plasma Sci. Technol., 2015, **17**, 649–655.

41 Y.-X. Fu, L. Wang and L. Xu, Open Phys., 2020, **18**, 40–47.

42 S. Zhang, X. Wang, M. He, Y. Jiang, B. Zhang, W. Hang and B. Huang, Spectrochim. Acta Part B At. Spectrosc., 2014, **97**, 13–33.

43 J. Hermann, C. Boulmer-Leborgne and D. Hong, J. Appl. Phys., 1998, **83**, 691–696.

44 J. . Aguilera and C. Aragón, Spectrochim. Acta Part B At. Spectrosc., 2004, **59**, 1861–1876.

45 I. B. Gornushkin, S. V. Shabanov and U. Panne, J. Anal. At. Spectrom., 2011, **26**, 1457.

46 E. Kepes, I. Gornushkin, P. Porizka and J. Kaiser, Anal. Chim. Acta, , DOI:10.1016/j.aca.2020.06.078.

View Article Online
DOI: 10.1039/D0AN01996H

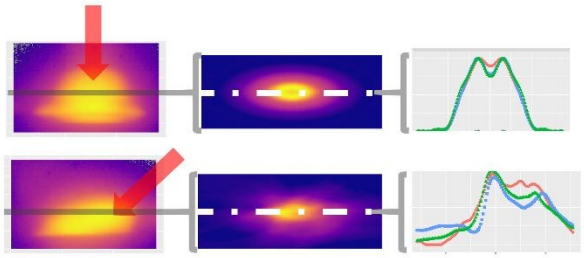

Plasmas induced with large ablation angles are less temporally stable and less spatially homogenous, which should be considered during quantitative analysis by laser-induced breakdown spectroscopy.